New Journal of Physics
The open access journal at the forefront of physics

Deutsche Physikalische Gesellschaft DPG
IOP Institute of Physics

Published in partnership with: Deutsche Physikalische Gesellschaft and the Institute of Physics

OPEN ACCESS

RECEIVED
4 June 2019

REVISED
14 October 2019

ACCEPTED FOR PUBLICATION
30 October 2019

PUBLISHED
25 November 2019

PAPER

Quantum electrodynamics with magnetic textures

María José Martínez-Pérez[1,2] **and David Zueco**[1,2]

[1] Instituto de Ciencia de Materiales de Aragón and Departamento de Física de la Materia Condensada, CSIC-Universidad de Zaragoza, Pedro Cerbuna 12, E-50009, Zaragoza, Spain
[2] Fundación ARAID, Avda. de Ranillas, E-50018, Zaragoza, Spain

E-mail: pemar@unizar.es **and** dzueco@unizar.es

Keywords: cavity quantum electrodynamics (QED), magnetic textures, quantum optics and magnetism

Abstract

Coherent exchange between photons and different matter excitations (like qubits, acoustic surface waves or spins) allows for the entanglement of light and matter and provides a toolbox for performing fundamental quantum physics. On top of that, coherent exchange is a basic ingredient in the majority of quantum information processors. In this work, we develop the theory for coupling between magnetic textures (vortices and skyrmions) stabilized in ferromagnetic nanodiscs and microwave photons generated in a superconducting circuit. Within this theory we show that this hybrid system serves for performing broadband spectroscopy of the magnetic textures. We also discuss the possibility of reaching the strong coupling regime between these texture excitations and a single photon residing in a microwave superconducting cavity.

1. Introduction

With the promise of developing quantum technologies, in the last years an enormous effort has been focused on building different quantum systems operating in a fully quantum coherent way [1]. Ion traps, quantum dots and superconducting circuits are prominent examples [2]. Thanks to this progress, it has been realised that combining different physical systems could help in optimising a quantum processor [3]. For example, we can imagine long decoherence spin qubit ensembles working as quantum memories. This ensemble could be coupled to superconducting transmission lines, where microwave photons can share the information between such a memory and the processing unit made of superconducting qubits. On the other way, merging different substances can serve to transduce between different type of quantum excitations. Examples of the latter are mechanical oscillations interacting with superconducting circuits or cavities [4, 5] or coupling surface acoustic waves and superconducting circuits [6, 7].

Another interesting interface would be that formed by spin waves and microwave photons. This is appealing since photons are well established in both quantum computing and communication architectures for mediating interactions between qubits and acting as information carriers, respectively. Spin waves (or their corresponding quasiparticles, magnons) are, on the other hand, their short-wavelength counterpart in spintronics. Based on their small wavelength, together with the absence of Ohmic dissipation, the field of magnonics aims to exploit spin waves to produce nanoscopic low-loss devices [8]. Different magnonic excitations have been proposed or have already been coupled to quantum light experimentally [9]. Most studies have focused on Yttrium–Iron–Garnet (YIG) films or spheres coupled to either superconducting coplanar waveguide (CPW) resonators [10, 11] or 3D cavities [12, 13]. The latter allows exciting mostly the uniform Kittel mode in which all spins precese in unison. Fewer works have analysed the case of higher-order spin wave modes in confined geometries [14–17] and individual magnetic solitons such as vortices in soft-magnetic discs [18, 19]. Magnetic vortices are extremely stable magnetic textures exhibiting a very rich dynamical behaviour in the sub-GHz to tens of GHz range. Vortices have been used, e.g. as spin-torque nanoscillators [20] or to generate ultrashort ($<$100 nm) spin waves [21, 22]. The latter application is enormously interesting for the implementation of magnonic devices as it would allow the emission of coherent, ultrashort spin waves of arbitrary wavelength.

In a previous work, we have proposed a set up where photons are coupled to the gyrotropic motion of a vortex in a ferromagnetic disc [19]. Importantly, we explored the possibility of reaching the so-called strong coupling regime. The latter means that quanta of vortex motion and photons are exchanged in a fully quantum coherent way, because the vortex-photon coupling is larger than both the material's damping and the photon leakage. In the present work, we generalise our proposal to include the coupling to higher-order vortex modes reaching the 15 GHz range. High-energy modes might lead to larger coupling factors because the intensity of the zero-point current fluctuations in a cavity depends linearly on its resonance frequency. This regime will also be very interesting for vortex-mediated generation of spin-waves that usually takes place within the 1–15 GHz range [21, 22].

We also consider the coupling of microwave photons to the characteristic breathing mode of a magnetic skyrmion confined in a thin magnetic disc. Skyrmions constitute a new paradigm in condensed matter physics [23]. These particle-like objects can reach the nanometer scale being very interesting logic units or memory bits [24]. Even more important for spintronics, skyrmions can be moved with record low-power electric currents [25]. Yet, their nucleation, stabilisation and manipulation is a very challenging task, especially in the absence of magnetic fields and at room temperature, as required for information applications [26].

As we will show here, strong coupling between microwave photons and high-order vortex modes is feasible. Even if the amplitude of these modes is considerably lower than that of the gyrotropic mode, this is compensated by the larger intensity of the electromagnetic fluctuations. Coupling between photons and the breathing mode peculiar to skyrmions is much more tricky. All these couplings are ultimately limited by the Gilbert damping of the ferromagnetic material. We will start by describing the spin Hamiltonian and the resulting stable magnetic textures. The rest of the paper is organised as follows. We introduce the theory for coupling magnetic textures to photons generated in superconducting circuits both in open transmission lines and single mode cavities. We review the different vortex modes and how to measure them by means of a transmission experiment. Finally, we explore the coupling regimes of both vortices and skyrmion modes to single cavity photons and discuss the feasibility of reaching the strong coupling regime.

2. Magnetic Hamiltonian and its coupling to light

2.1. Magnetic textures

The spin Hamiltonian of a ferromagnet can be written as:

$$H_S = H_{\rm ex} + H_{\rm dip} + H_{\rm K} + H_{\rm DMI} + H_{\rm Z}. \tag{1}$$

Here, $H_{\rm ex} = -J_{ij}\vec{S}_i\,\vec{S}_j$ is the Heisenberg exchange energy, $H_{\rm dip}$ is the dipolar term that accounts for the total magnetostatic energy of the system (shape anisotropy), $H_{\rm K}$ is the magnetocrystalline anisotropy that sets some preferred axis for the magnetization and $H_{\rm DMI} = D_{ij}\vec{S}_i \times \vec{S}_j$ is the Dzyaloshinskii–Moriya interaction (DMI) term, with D_{ij} the strength of the asymmetric interaction. Finally, $H_Z = g_{\rm e}\mu_{\rm B}\overrightarrow{B}(\mathbf{r}_i)\overrightarrow{S_i}$ is the Zeeman coupling between spins and the externally applied magnetic field $\vec{B}(\mathbf{r}_i)$. $\vec{S}_i = (S_i^x,\, S_i^y,\, S_i^z)^t$ are spin-angular momentum operators, $g_{\rm e}$ is the electron g-factor and $\mu_{\rm B}$ is the Bohr magneton. The spin operators satisfy $[S_i^\alpha,\, S_j^\beta] = {\rm i}\delta_{ij}\,\epsilon_{\alpha\beta\gamma}S^\gamma$ with $\alpha, \beta, \gamma = x, y, z$. The exchange length $\lambda_{\rm ex}$ defines the characteristic length scale of the magnetic textures under study.This amounts to $\lambda_{\rm ex} \sim 5$ nm typically, being much smaller than the dimensions of the nanodiscs where they are stabilized. Under these conditions, quantum fluctuations can be neglected and the equations of motion for the average magnetic moment, i.e. $\vec{\mu}_j = g_{\rm e}\mu_{\rm B}\langle\vec{S}_j\rangle$, can be casted in the Landau–Lifshitz-Gilbert (LLG) equation [27, 28]:

$$\frac{\partial\vec{\mu}_j}{\partial t} = \frac{\gamma_e}{1+\alpha_{\rm LLG}^2}\left\{\vec{\mu}_j \times \vec{B}_{\rm eff} + \frac{\alpha_{\rm LLG}}{\mu_{\rm B}}[\vec{\mu}_j \times (\vec{\mu}_j \times \vec{B}_{\rm eff})]\right\}. \tag{2}$$

Here, $\vec{\mu}_j = (\mu_j^x,\, \mu_j^y,\, \mu_j^z)$, γ_e is the electron gyromagnetic ratio, $\alpha_{\rm LLG}$ is the dimensionless Gilbert damping of the material, and $\vec{B}_{\rm eff}$ is an effective field that accounts for all terms considered in the spin Hamiltonian (1).

Depending on the magnetic object under study (material, size and shape) and the initial conditions (or the magnetic history), relaxing equation (2) leads to the stabilisation of different magnetic textures. These might have very interesting properties such as topological protection. Two archetypal textures are the magnetic vortex and the skyrmion. The former is the ground magnetic state in flat micro- or nanoscopic magnetic discs with negligible magnetocrystalline anisotropy (i.e. $H_{\rm K} = 0$ and $H_{\rm DMI} = 0$ in the spin Hamiltonian (1)). The minimisation of surface magnetic charges makes spins lie preferentially parallel to the borders of the disc, leading to the characteristic vortex spin curling in clockwise or counterclockwise fashion, as shown in figure 1(a). In the vortex core, spins turn out-of-plane pointing up or down defining the vortex polarity [29]. This yields four possible states that are, in principle, degenerate. The lowest energy excitation peculiar to vortices

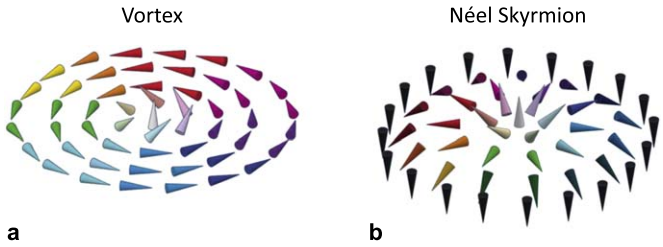

Figure 1. Schematic representation of the spatial distribution of magnetic moments typical of (a) a vortex or (b) a Néel skyrmion confined in thin magnetic discs.

is the gyrotropic mode, in which the vortex core gyrates around its equilibrium position. It is predominantly excited by means of an in-plane oscillating magnetic field.

Skyrmion stabilization is a little more tricky, since it requires the presence of terms favouring non-collinear spin ordering such as the DMI (i.e. $H_{\rm DMI} \neq 0$ in the spin Hamiltonian (1)). Néel-like skyrmions can be typically stabilized in confined geometries such as flat micro- or nanodiscs by means of the interfacial-DMI. This interaction arises in multilayers where ultra-thin ferromagnets are combined with materials having large spin–orbit coupling [24]. Additionally, a preferred out-of-plane magnetic ordering is required. The latter is usually achieved by the application of external magnetic fields, or by using materials with perpendicular magnetic anisotropy (i.e. $H_{\rm K} \neq 0$ in the spin Hamiltonian (1)). Skyrmions are characterised by a central core pointing in the opposite direction to the surrounding magnetization, so that spins can be projected once onto the unit sphere (see figure 1(b)). Using perpendicular (out-of-plane) oscillating fields it is possible to excite the breathing mode peculiar to the skyrmion, in which it conserves radial symmetry [30].

2.2. Light–matter Hamiltonian

The objective of this work is to study the coupling between vortex or skyrmion excitations and photons. In particular, photons generated by currents in superconducting circuits, either propagating in transmission lines or stationary photons living in cavities. The total Hamiltonian, including the magnetic nanodisc, the electromagnetic field and their interaction is decomposed as:

$$H_T = H_S + H_Q + H_I. \tag{3}$$

Here, H_S is the spin Hamiltonian (see equation (1)) and H_Q is the photonic Hamiltonian. In the case of one dimensional (1D) transmission lines it reads [31];

$$H_Q = \hbar \int {\rm d}\omega\ \omega\ r_\omega^\dagger r_\omega + \hbar \int {\rm d}\omega\ \omega\ l_\omega^\dagger l_\omega, \tag{4}$$

where $[r_\omega,\ r_{\omega'}^\dagger] = \delta(\omega - \omega')$ are right-moving modes while $[l_\omega,\ l_{\omega'}^\dagger] = \delta(\omega - \omega')$ are the left-moving ones. Here, we are considering 1D fields where the k index stands for the photon wavenumber for the transverse mode solutions of the wave equations. Owing to the fact that light propagates in 1D (z with our choice, see figure 2), we know that $\omega_k = vk$ with v the propagation velocity. In transmission lines $v = \sqrt{1/LC}$ with L (C) being the effective inductance (capacitance) per unit of length.

H_I is the Zeeman coupling between the magnetic moments and the magnetic field $\vec{B}(\mathbf{r})$ generated by the circuit:

$$H_I = -g_{\rm e}\mu_{\rm B} \sum_i \vec{\mathcal{S}}_i\, \vec{B}(\mathbf{r}_i). \tag{5}$$

Finally, the magnetic field at point $\mathbf{r} = (x, y, z)$ is quantized in the Coulomb gauge as [32, ch 10]:

$$\vec{B}(\mathbf{r}) = \sqrt{\frac{\hbar}{2vc^2\epsilon_0}} \begin{pmatrix} \mathcal{B}_x(x,\ y) \\ \mathcal{B}_y(x,\ y) \\ 0 \end{pmatrix} \int {\rm d}\omega \sqrt{\omega} (r_\omega^\dagger {\rm e}^{{\rm i}\omega z/v} + l_\omega^\dagger {\rm e}^{-{\rm i}\omega z/v} + {\rm h.c.}). \tag{6}$$

Here, h.c. means hermitean conjugate, $\mathcal{B}_x$ ($\mathcal{B}_y$) are the transverse x (y) components of the field density having units of inverse length, c is the speed of light in vacuum and ϵ_0 is the vacuum permittivity. We emphasise that we are mainly interested in discussing the single photon coupling. Thus, these components must be understood as the *root mean square* value of the field ($\vec{b}_0$) generated by the vacuum current fluctuations in the circuit ($i_{\rm rms}$). In section 3 we explain how to compute them. Experimentally, the single photon regime can be achieved at very low temperatures (i.e. few mK) and upon severe attenuation of the input/output signal lines.

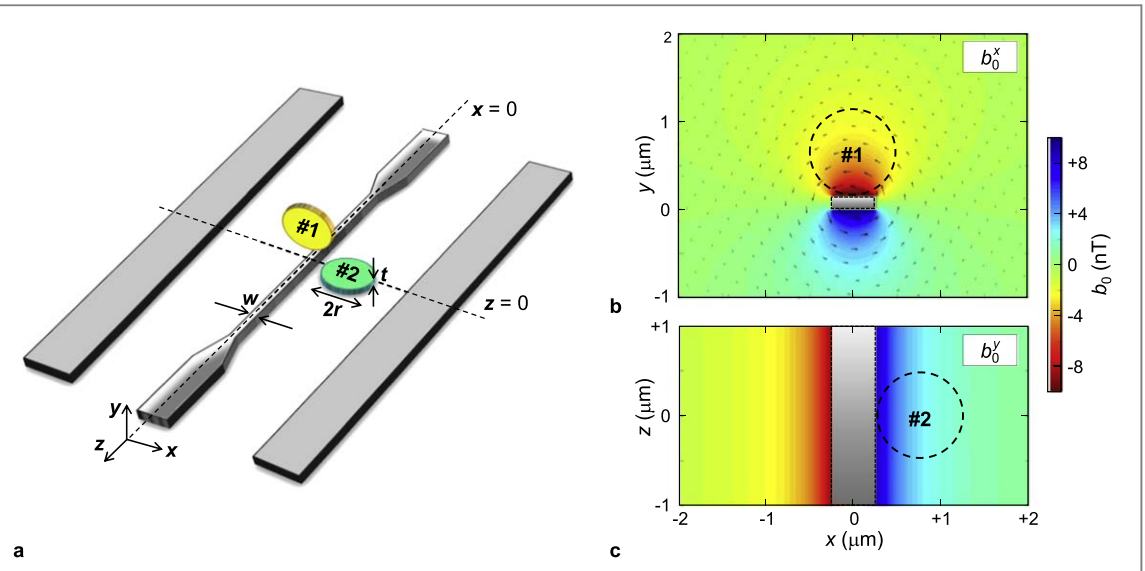

Figure 2. (a) Scheme of the proposed experiment. The relevant dimensions and the coordinate axes are highlighted. Two different disc locations are considered, #1 and #2. These correspond to the rms excitation field applied in-plane and out-of-plane of the disc, respectively. $2r$ is the disc diameter, t the thickness and w the constriction width. (b) and (c) show the numerically calculated density plots of the x and y components of the rms field along the discs #1 and #2, i.e. planes $z = 0$ and $y = 0$, respectively. In the calculations we assume a zero-point current $i_{\rm rms} = 11$ nA flowing through a superconducting constriction with $w = 500$ nm and thickness 150 nm.

2.3. Waveguide quantum electrodynamics

Quantum systems coupled to 1D bosonic fields, as in equations (5) and (6),are of high interest. They are named waveguide quantum electrodynamics (QED) to differentiate them from cavity-QED setups, where the quantum system is coupled to the discrete stationary modes of a cavity. 1D waveguides are used to enhance the light and matter coupling in order to, e.g. mediate effective interactions between spatially separated quantum systems or to generate or manipulate quantum states of light as single or N-photon wavepackets. Here, we use this waveguide QED setup to perform broadband spectroscopy of magnetic textures.

An ideal experimental setup for resolving the excitation spectrum of magnetic nanodiscs will use the field fluctuations in a waveguide b_0 as the perturbation field, as sketched in figure 2(a). Owing to the continuum spectrum of the waveguide (using superconducting circuits, the operation range can be safely assumed to lie between few MHz up to 15–20 GHz) we can access all characteristic modes in a single experiment. In particular, the excitation spectrum can be obtained by measuring the transmission through the superconducting waveguide. To see how it works, we study the dynamics of a nanodisc coupled to a waveguide through equation (5). We highlight that we will consider two locations, i.e. position #1 and position #2 in figure 2(a). The former will be used to excite modes susceptible to in-plane magnetic fields. On the other hand, position #2 will be used to excite modes susceptible to an out-of-plane excitation. In both cases, the rms field is negligible along the z direction ($b_0^z \sim 0$).

The field fluctuations on the waveguide can be estimated numerically in the following way. We assume that a total current $i_{\rm rms}$ is circulating through the superconducting transmission line with given width w and thickness. The spatial distribution of $i_{\rm rms}$ is calculated using the software 3D-MLSI that allows one to solve the London equations in thin film superconducting wires [33]. We then use the same software to compute the spatial distribution of $\vec{b}_0$ generated by $i_{\rm rms}$. As an example, we use $i_{\rm rms} = 11$ nA and assume a Nb central transmission line with a constriction of width $w = 500$ nm and thickness 150 nm (see section 3.1 for more details about the constriction). Figures 2(b) and (c) show the resulting density plots of b_0^x and b_0^y along the $z = 0$ and $y = 0$ planes corresponding to positions #1 and #2, respectively. As it can be seen, the excitation magnetic field $\vec{B}(\mathbf{r}) = \vec{b}_0$ is non-homogeneous along the surface of the disc located at both locations #1 and #2. However, to simplify calculations we will approximate $\vec{B}(\mathbf{r})$ to the one passing through the disc centre (core of the topological solution), i.e. $\vec{B}(\mathbf{r}) \cong \vec{B}(\mathbf{r}_c)$, with $\mathbf{r}_c$ the centre of the nanodisc. As we will see in section 3.1, this is a good approximation for the first resonant modes of both vortices and skyrmions. For a disc located at position #1 (#2), $\vec{B}(\mathbf{r}_c)$ has only x (y) component. Accordingly, $\vec{B}(\mathbf{r}) \cong B^x(\mathbf{r}_c) = b_0^x(\mathbf{r}_c)$ at position #1 whereas $\vec{B}(\mathbf{r}) \cong B^y(\mathbf{r}_c) = b_0^y(\mathbf{r}_c)$ at position #2. Consequently, we can write a simplified total coupling Hamiltonian

$$H_T = H_S + H_Q + \sum_j S_j^\alpha \int \mathrm{d}\omega\ \lambda_\alpha(\omega)\,(\mathrm{e}^{\mathrm{i}\omega z/v} r_\omega^\dagger + \mathrm{e}^{-\mathrm{i}\omega z/v} l_\omega^\dagger + \mathrm{h.c.}), \tag{7}$$

with $\lambda_\alpha(\omega) = \sqrt{\frac{\hbar}{2vc^2\epsilon_0}}\mathcal{B}_\alpha(x_c, y_c)\sqrt{\omega_k}$ and $\alpha = x$ and y for positions #1 and #2, respectively.

So far, we have just written the Zeeman coupling (5) in a convenient way by using the quantized field in the waveguide, see equation (6). This is rather general, but we are interested in the coupling to magnetic textures and, in particular, in resolving their excitation spectrum in a transmission experiment. This facilitates the job, since it is known that using linear response theory[3] and input–output theory it is possible to find the scattering matrix. For the transmission function this results in [34]:

$$T(\omega) = 1 - \sum_i \frac{\Gamma(\omega_n)}{\Gamma(\omega_n) + \Delta\omega_n + \mathrm{i}(\omega_n - \omega)}, \tag{8}$$

while the reflection is given by $R(\omega) = T(\omega) - 1$. The transmitted (reflected) measured power is given by $|T(\omega)|^2$ ($|R(\omega)|^2$). Here, ω_n are the resonant frequencies of the different normal modes (n) of the magnetic texture whereas $\Delta\omega_n$ are their corresponding linewidths (being proportional to α_{LLG}). $\Gamma(\omega_n)$ is the emission rate of the texture in the waveguide which depends on $\lambda_\alpha(\omega)$. Its exact calculation is based, in principle, in knowing the analytic solution for the magnetic textures, which is not possible in general. However, it is always possible to compute it numerically as we will explain in section 3.

2.4. Numerical simulations and normal modes

In this section we compute $|T(\omega)|$ numerically for a model soft magnetic disc in the absence of both DMI and magnetocrystalline anisotropy. This is to say, we restrict ourselves to the study of the normal modes peculiar to magnetic vortices. Simulations are performed using the GPU-accelerated code MuMax[3] [35]. We consider a disc with radius $r = 500$ nm and thickness $t = 80$ nm. Finally, for a more general discussion, we assume prototype material parameters.

The saturation magnetization of conventional ferromagnets, e.g. Fe or $Ni_{80}Fe_{20}$ (Py), amounts to $M_s \sim 1.7$ MA m^{-1} and $M_s \sim 0.8$ MA m^{-1}, respectively [36]. Other interesting candidate is YIG with a very reduced $M_s \sim 0.14$ MA m^{-1} [37]. Finally, much attention is currently being pay to ferromagnetic composites like Heusler alloys or Co_xFe_{1-x}. For example, NiMnSb exhibits $M_s \sim 0.85$ MA m^{-1} whereas the saturation magnetization of Co_xFe_{1-x} amounts to $M_s \sim 2.4$ MA m^{-1} for $x = 0.25$ [38, 39]. Typical values of the exchange stiffness constant are $A(\mathrm{Fe}) = 21$ pJ m^{-1}, $A(\mathrm{Py}) = 13$ pJ m^{-1}, $A(\mathrm{YIG}) = 1.9$ pJ m^{-1}, $A(\mathrm{NiMnSb}) = 9.0$ pJ m^{-1} and $A(Co_{0.25}Fe_{0.75}) = 26$ pJ m^{-1}. Finally, very low α_{LLG} values can be currently achieved using low damping ferromagnets like the above mentioned Heusler and Co_xFe_{1-x} alloys reaching 10^{-3} and 5×10^{-4}, respectively [38, 39]. Typical ferromagnetic metals such as Fe and Py exhibit larger α_{LLG} of the order of 2×10^{-3} and 8×10^{-3}, respectively [36]. Currently, record low damping values are reported for the insulating ferrimagnet YIG, having $\alpha_{\mathrm{LLG}} \sim 5 \times 10^{-5}$, although at the cost of a largely reduced saturation magnetization [37]. With this considerations in mind we set $M_s = 1$ MA m^{-1}, $A_{\mathrm{ex}} = 15$ pJ m^{-1} and $\alpha_{\mathrm{LLG}} = 10^{-3}$. These values yield a total exchange length $\lambda_{\mathrm{ex}} = \sqrt{2A_{\mathrm{ex}}/\mu_0 M_s} \sim 5$ nm, typical of conventional ferromagnets.

The excitation spectrum of the prototype ferromagnetic disc is obtained by applying a perturvative field $B^\alpha(\tau) = A\ \mathrm{sinc}(\omega_{\mathrm{cutoff}}\tau)$ with amplitude $A = 1$ mT and $\omega_{\mathrm{cutoff}}/2\pi = 50$ GHz. Calculating the Fast Fourier Transform (FFT) of the resulting spatially-averaged time-varying magnetization along the field direction results in the spectrum plotted in figure 3(a) (bottom panel). The black curve results when applying an in-plane driving field (i.e. $\alpha = x$, position #1) whereas the red one corresponds to an out-of-plane excitation (i.e. $\alpha = y$, position #2). Each peak corresponds to a normal mode of the ferromagnetic disc labelled g1, g2, a1, a2, a3 and r. Fitting each resonance peak to a Lorentzian function allows estimating ω_n and $\Delta\omega_n$ with $n = \{\mathrm{g1}, \mathrm{g2}, \mathrm{a1}, \mathrm{a2}, \mathrm{a3}$ and $\mathrm{r}\}$. These values, together with the estimated $\Gamma(\omega_n)$ computed in section 3.1, are plugged into equation (8) resulting in the transmission curve plotted in figure 3(a) (top panel).

We calculate now the spatial distribution of the amplitude of the FFT of the spatially-resolved time-varying magnetization. The resulting plots can be seen in figure 3(b) for the upper and bottom disc surfaces and the transverse cut. This representation helps to visualise the magnetization profile of each mode that we describe in the following. The lowest energy mode (g1) corresponds to the vortex core translation around the central position. The gyration sense is only given by the vortex polarity regardless the direction of the in-plane magnetization which plays no role. This is the archetypal gyrotropic mode where the vortex core is only minimally distorted through the disc thickness, as it can be seen in the transverse cut shown in figure 3(b). At slightly larger energy, we observe the second gyrotropic mode (g2) where the vortex gyrates in the upper/bottom disc surface with a π phase shift. In this way, the vortex core itself flexes through the disc thickness yielding one node in the centre. This node can be easily appreciated in the transverse cut shown in figure 3(b). Several

[3] The input signal is weak so we assume that the magnetic texture is excited within the linear regime.

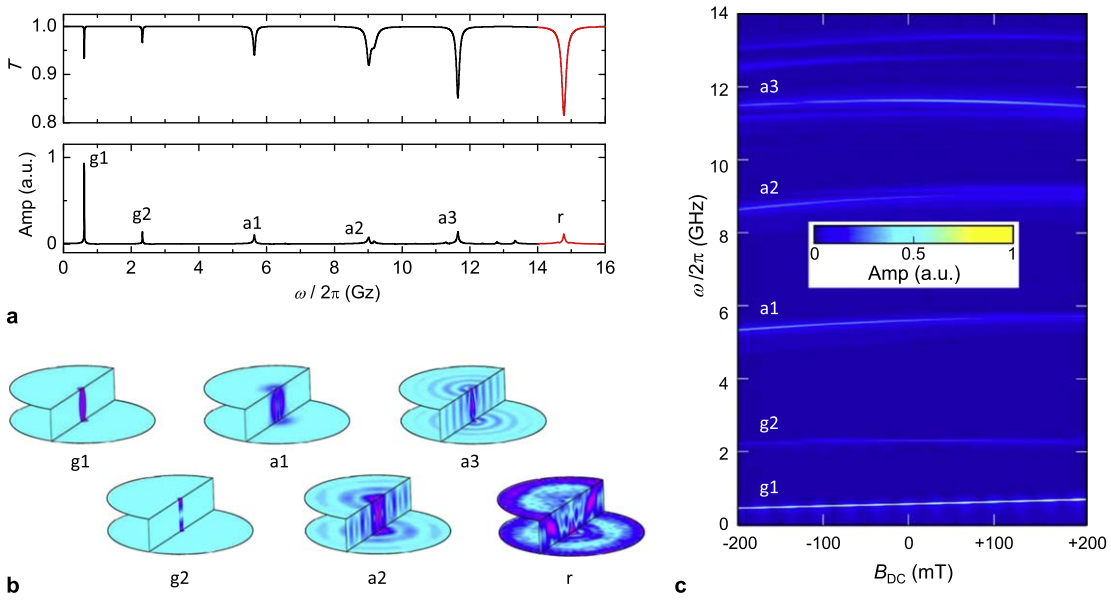

Figure 3. Resonant modes of a typical magnetic disc with $r = 500$ nm and $t = 80$ nm. We use the following notation: 'g' stands for gyrotropic, 'a' denotes the azimuthal modes whereas 'r' refers to the radial mode. (a) Numerically calculated transmission and FFT of the magnetisation response to an excitation magnetic field. The black (red) curve is the response to an in-plane (out-of-plane) oscillating magnetic field. (b) Spatial distribution of the amplitude (in arbitrary units) of the FFT of the spatially-resolved time-varying magnetization calculated for the the top/bottom surfaces of the disc and a transverse cut corresponding to the different modes. (c) Dependence of the resonant frequencies on the application of a DC out-of-plane mangetic field B_{DC}. Only modes excited by an in-plane excitation field are shown.

azimuthal modes (a1, a2 and a3) can be observed as well. Here, the vortex core also gyrates but there is an additional magnetization spiral that shows up in the upper/bottom surface plots in figure 3(b). This spiral breaks radial symmetry and exhibits a increasing number of nodes along the radial direction for increasing mode number. Importantly, these modes are not homogeneous trough the disc thickness but curl at opposite directions from top to the bottom surfaces [40]. Finally, in the case of an out-of-plane excitation field one finds a dominant mode conserving radial symmetry (r). As shown in figure 3(b), this mode is neither homogeneous through the disc thickness.

The energy of each mode can be slightly tuned by means of an external DC magnetic field B_{DC}. This can be seen in figure 3(c), where the energy spectrum is plotted against B_{DC}. Curves are calculated for an out-of-plane field applied along the same direction as the vortex core magnetization. The gyrotropic mode increases linearly with the applied magnetic field whereas higher energy modes exhibit a non-monotonous behaviour. The presence of other low-amplitude resonant modes can be appreciated as well. This is the case of, e.g. modes visible between 12 and 14 GHz that will not be studied here.

3. Magnetic textures and cavity QED: strong and weak coupling regimes

Shunting the transmission line by two capacitors, it is possible to confine the electromagnetic field. These capacitors act as mirrors creating a microwave realisation of a Fabry–Pérot cavity. The boundary conditions at the capacitors impose the frequency quantization for the photonic modes inside the cavity, namely $\omega_C = v\pi/ln$, with l the cavity length (the distance between the capacitors). Besides, we notice that if the cavity contains few photons, ultimately only one, it is safe to assume that the topological solution is perturbed within the linear response regime. In such a case, the dynamics of the magnetic texture can be cast in a harmonic-oscillator-like equation of motion [41, 42]. Therefore, the texture magnetization is written as,

$$M_n = \Delta M_n (b_n^\dagger + b_n). \tag{9}$$

Here, $\Delta M_n = \sqrt{\langle \Delta M_n^2 \rangle - \langle M_n^2 \rangle}$, where $\langle ... \rangle$ are averages over the ground state. This can be calculated by computing the maximum response in magnetization when the vacuum field fluctuations b_0 drive the magnetic texture at resonance. Putting all together, the texture excitations coupled to a single mode cavity can be written in it simplest form as two coupled harmonic modes

$$H \cong \hbar\omega_C a^\dagger a + \hbar \sum_n \omega_n b_n^\dagger b_n + \hbar g_n (b_n^\dagger + b_n)(a^\dagger + a). \tag{10}$$

Here, the coupling strength [19]:

$$g_n = \frac{b_0^\alpha(\mathbf{r}_c)}{2}\sqrt{\frac{V\ \chi^\alpha(\omega_n)\ \Delta\omega_n}{\hbar}}, \tag{11}$$

with $\chi^\alpha(\omega_n) = \Delta M_n^\alpha / b_0^\alpha(\mathbf{r}_c)$ the magnetic susceptibility at resonance for each mode. We refer the reader to [19] where we explained in detail how to arrive to equation (11).

The most fundamental figure of merit in cavity QED is the ratio between g and the dissipative rates, namely the resonance linewidth ($\Delta\omega_n$) which is proportional to the material damping $\alpha_{\rm LLG}$ and the cavity leakage (κ). If the coherent coupling g exceeds both dampings one lies within the strong coupling regime [43]. In this way, it is possible to entangle photons and resonant magnetic modes. This serves to use the cavity photons as a quantum bus among two or more nanodiscs, or to perform a transducer between microwave photons and spin waves. To estimate if this regime is reachable, the spin excitations and photons must exchange populations coherently in the form of vacuum Rabi oscillations before they are damped out. The condition to have such oscillations is given by: $4g_n > |\kappa - \Delta\omega_n|$ [44, 45]. In our case, κ can reach the Hz range easily, whereas typical ferromagnetic materials exhibit $\Delta\omega_n \sim$ MHz at best. Therefore, throughout this work, we are interested in checking if

$$4g_n > \Delta\omega_n \tag{12}$$

is possible.

3.1. Numerical simulations

To obtain the coupling g_n we proceed as follows. We fix our attention to a half-wavelength CPW resonator, where a central superconducting line of a few microns is surround by two ground planes. The geometry of this experiment is similar to that sketched in figure 2(a) for the case of a transmission line. In the present case, two capacitors are used to confine the photons inside the resonator yielding different quantized modes with frequency $\omega_C = \omega_n$. First, we need to compute the rms of the zero point current fluctuations flowing through the central conductor:

$$i_{\rm rms} = \omega_C \sqrt{\frac{\hbar\pi}{2Z_0}}, \tag{13}$$

with $Z_0 = 50\,\Omega$ the typical impedance of the resonator.

The spatial distribution of $i_{\rm rms}$ is calculated using the software 3D-MLSI as described in section 2.3. This current generates a field $\vec{B}(\mathbf{r})$ that is used to compute b_0 at the centre of the nanodisc. Besides, $\vec{B}(\mathbf{r})$ also serves to excite the topological solution. Therefore, we use a perturvative field $B^\alpha(\tau) = b_0^\alpha(\mathbf{r}_c)\sin(\omega\tau)$ and compute the resulting maximum response in magnetization ΔM_n^α for each mode n. Here, $\alpha = x$ for position #1 whereas $\alpha = y$ for position #2. Approximating the non-homogeneous rms field to the one produced at the centre of the nanodisc is a good approximation for the gyrotropic, first azimuthal modes and the breathing mode peculiar to skyrmions. This is so since the magnetization modulation concentrates mostly on the disc's central region (see figure 3(b)). This is not the case of higher-order azimuthal and radial modes. In these cases, however, our approach underestimates the resulting ΔM_n by a factor ~1.5 only, as checked numerically. The coupling is finally calculated using equation (11). Finally, it remains to compute the rate $\Gamma(\omega_n)$ appearing in the transmission equation (8). This can be done using the relation between the waveguide-resonator coupling [46]:

$$g_n = \sqrt{\frac{\Gamma(\omega_n)\omega_n}{\pi}}. \tag{14}$$

In the simulations, we assume that a constriction of width w is patterned in the central conductor to increase the strength of the resulting b_0 field. The reader is referred to figure 2 for the definition of w and to [47] and [19] for a discussion on the increase of the coupling strength using nanoconstrictions. In our calculations, $w = 500$ nm (in a 150 nm thick Nb central conductor) for the magnetic vortex whereas $w = 50$ nm (in a 50 nm thick Nb conductor) for the skyrmion.

In the case of the vortex, we consider a disc with radius $r = 500$ nm and thickness $t = 80$ nm and prototype material parameters, i.e. $M_s = 1$ MA m^{-1} and $A_{\rm ex} = 15$ pJ m^{-1}. We let the damping vary between $10^{-4} < \alpha_{\rm LLG} < 10^{-2}$. We highlight that coupling to each normal mode is calculated assuming a different CPW resonator with characteristic frequency $\omega_C = \omega_n$, with $n = \{$g1, g2, a1, a2, a3, r and s$\}$. In figure 4 we plot the resulting strong coupling condition given by equation (12) for the different resonant modes and for different values of the damping parameter. The coupling condition depends linearly on $\alpha_{\rm LLG}$, increasing for decreasing damping parameter. Interestingly, although ΔM_n decreases for high order modes, all of them exhibit similar values of the coupling condition, increasing slightly for increasing frequency. This is due to the fact that the

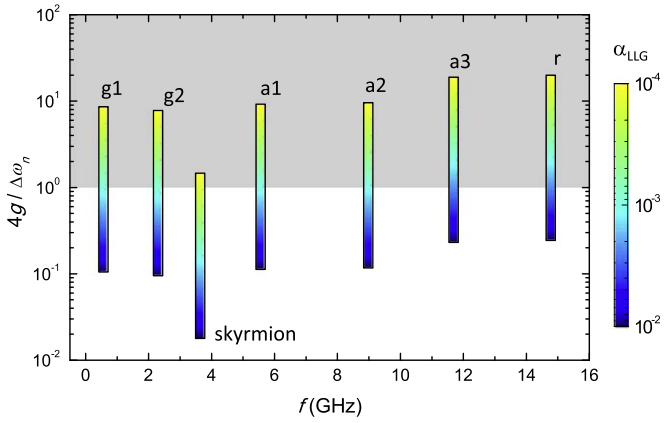

Figure 4. Numerically calculated coupling condition (see equation (12)) for the different resonant modes of the vortex and skyrmion textures. The strong coupling condition increases linearly with decreasing $\alpha_{\rm LLG}$. The shadowed (white) region corresponds to strong (weak) coupling. These serve to highlight the possibility of reaching strong coupling for all resonant modes of the vortex texture provided the damping is low enough.

reduced ΔM_n is compensated by an increased strength of the zero-point current fluctuations at larger frequencies, see equation (13). Additionally, $\Delta\omega_n$ also increases for increasing mode number as $\Delta\omega_n \propto \alpha_{\rm LLG}\omega_n$. Finally, we highlight that the coupling strength is independent of the vortex polarity (up/down) and circulation (clockwise/counterclockwise).

For the disc size analysed here, using materials with low $\alpha_{\rm LLG} \sim 10^{-3}$ will assure reaching the strong coupling regime for all resonant modes. This is well within the current state-of-the-art using low-damping ferromagnets like Heusler alloys or CoFe. Using the latter material, even larger coupling factors are expected stemming from its large saturation magnetisation. Moreover, the reported value of $\alpha_{\rm LLG} \sim 5 \times 10^{-4}$ was measured for a very thin 10 nm thick $Co_{0.25}Fe_{0.75}$ film at room-temperature [39]. This means that even lower damping parameters could result in the proposed ferromagnetic disc ($t = 80$ nm) and working at very low temperatures (mK range).

These numbers can be compared with the expected strong coupling condition for an uniformly magnetised thin-film. For this purpose, we assume a 5 nm thick 1 μm $\times$ 13 μm magnet, which yield the same volume as that of the disc used for vortex stabilisation. We also assume the same material parameters, i.e. $M_{\rm s} = 1$ MA m^{-1}, $A_{\rm ex} = 15$ pJ m^{-1} and $\alpha_{\rm LLG} = 10^{-3}$. The thin-film lies on top of a $w = 1$ μm constriction on a Nb conduction line (with thickness 150 nm). The resonator produces a relatively homogeneous magnetic field b_0 along the x direction (as for position #1, see figure 1(a)). Finally, an external bias magnetic field $B_{\rm DC}$ is applied along the z direction (long side of the magnet). Under these circumstances the uniform Kittel mode will be excited in the thin-film, the frequency of which is related to $B_{\rm DC}$ as $\omega_{\rm Kittel} \cong \gamma_e\sqrt{B_{\rm DC}(B_{\rm DC} + \mu_0 M_{\rm s})}$ [48]. Numerical simulations yield $4g/\Delta\omega_{\rm Kittel} \sim 3$, depending very smoothly on $\omega_{\rm Kittel}$. This is of the same order of magnitude as $4g/\Delta\omega_n \cong \{0.95,\ 0.85,\ 1.0,\ 1.1,\ 2.1,\ 2.3\}$ obtained for $n = \{$g1, g2, a1, a2, a3 and r$\}$, respectively, when assuming $\alpha_{\rm LLG} = 10^{-3}$. We highlight that excitation of the Kittel mode involves precession of *all* magnetic moments at unison. In contrast, the gyrotropic and first azimuthal modes cause a sizeable magnetization modulation in a very small region of the nanomagnet (disc's centre).

Regarding the skyrmion, we will focus on thin-film nanodiscs with perpendicular anisotropy and interfacial-DMI. Under these circumstances, a Néel skyrmion can be stabilized in the absence of an external bias magnetic field [49–52]. We will assume a thin multilayer disc with $r = 50$ nm and $t = 1$ nm. Material parameters given in the literature for systems allowing skyrmion stabilisation can vary significantly. For example, $M_{\rm s} = 0.6$ MA m^{-1}, $A_{\rm ex} = 15$ pJ m^{-1} and perpendicular magnetic anisotropy constant $K_u = 0.8$ MJ m^{-3} or $M_{\rm s} = 1.4$ MA m^{-1}, $A_{\rm ex} = 27$ pJ m^{-1} and $K_u = 1.4$ MJ m^{-3} are used for Pt/Co bilayers [49, 50]. Regarding the interfacial DMI strength D_i, it usually varies between 2 mJ m^{-2} $< D_i <$ 6 mJ m^{-2}. In our simulations we use $M_{\rm s} = 1$ MA m^{-1}, $A_{\rm ex} = 15$ pJ m^{-1}, $K_u = 1$ MJ m^{-3} and $D_i = 3$ mJ m^{-2}. Finally, in order to keep consistency with numerical results obtained for the vortex, we let the damping vary between $10^{-4} < \alpha_{\rm LLG} < 10^{-2}$.

Reaching strong coupling with the skyrmion is much more difficult. The strong coupling condition for the breathing mode peculiar to skyrmions lies almost one order of magnitude below that for the vortex (see figure 4). This is mostly due to the smallness of the disc used in the simulations. Ultra-thin films are required to obtain sizeable perpendicular anisotropy constants and interfacial DMI, limiting enormously the maximum thickness of the structures with skyrmionic ground states ($t \sim 1$ nm). In addition to that, ultra-thin films usually yield damping parameters in the $\alpha_{\rm LLG} \sim 0.1$ range. With these considerations in mind we can conclude that reaching

the strong coupling condition using skyrmions in state-of-the-art thin film multilayers would require strongly increasing the intensity of the zero-point field fluctuations in the cavity. Increasing b_0 can be achieved by patterning even narrower constrictions or by using low-impedance cavities [47]. A different possibility would imply using low-damping materials for skyrmion stabilisation. For instance, promising values of $\sim 3 \times 10^{-4}$ have been recently reported in bismuth doped YIG showing large perpendicular anisotropy [53].

4. Conclusions

Starting from the light–matter Hamiltonian, we have calculated the coupling of vortex and skyrmion modes to both propagating and cavity photons. Assuming typical material parameters, we have shown that the different modes can be distinguished in a transmission experiment using superconducting transmission lines. Importantly, we have also demonstrated that strong coupling between the different vortex modes in a nanodiscs and a single photon in a superconducting resonator is feasible within current technology. For this purpose, low-damping materials such as Heusler and CoFe alloys are paramount. On the other hand, reaching the strong coupling regime with skyrmion modes is much more challenging. This is due to the conditions imposed on the materials and the thickness of the films where skyrmionic states can be stabilized. The latter requires the use of ultra-thin ferromagnets that come along with high dampings and small thickness. To summarise, we have generalised our previous theory (see [19]), that was developed for the gyrotropic mode peculiar to vortices and single cavity photons, to provide a unified picture. In this way, we can treat now the coupling between whatsoever magnetic resonant mode and propagating or cavity photons.

The coupling between resonant modes occurring in vortex or skyrmion states might be important to transduce microwave photons to spin waves and vice versa. The latter are appealing due to their short wavelength that would enable to manipulate information in low-loss nanoscopic devices. Additionally, coherent coupling between different magnetic textures located in different regions of a CPW cavity would be feasible. This would allow phase-locking distant magnetic nanoscillators. Finally, photons could also be used to mediate the coupling between magnetic excitations and superconducting qubits located in the cavity [9].

Acknowledgments

We acknowledge support by the Spanish Ministerio de Ciencia, Innovación y Universidades, within projects MAT2015-73914- JIN, MAT2015-64083-R, and MAT2017-88358-C3-1-R, the Aragón Government project Q-MAD, and EU-QUANTERA project SUMO. We are grateful to Esteban Gutiérrez Mlot and Charles Downing for fruitful discussions.

References

[1] Acín A *et al* 2018 *New J. Phys.* **20** 080201
[2] Ladd T D, Jelezko F, Laflamme R, Nakamura Y, Monroe C and O'Brien J L 2010 *Nature* **464** 45–53
[3] Xiang Z L, Ashhab S, You J Q and Nori F 2013 *Rev. Mod. Phys.* **85** 623–53
[4] O'Connell A D *et al* 2010 *Nature* **464** 697–703
[5] Verhagen E, Deléglise S, Weis S, Schliesser A and Kippenberg T J 2012 *Nature* **482** 63–7
[6] Gustafsson M V, Aref T, Kockum A F, Ekstrom M K, Johansson G and Delsing P 2014 *Science* **346** 207–11
[7] Manenti R, Kockum A F, Patterson A, Behrle T, Rahamim J, Tancredi G, Nori F and Leek P J 2017 *Nat. Commun.* **8** 975
[8] Chumak A V, Vasyuchka V I, Serga A A and Hillebrands B 2015 *Nat. Phys.* **11** 453–61
[9] Lachance-Quirion D, Tabuchi Y, Gloppe A, Usami K and Nakamura Y 2019 *Appl. Phys. Express* **12** 070101
[10] Huebl H, Zollitsch C W, Lotze J, Hocke F, Greifenstein M, Marx A, Gross R and Goennenwein S T B 2013 *Phys. Rev. Lett.* **111** 127003
[11] Morris R G E, van Loo A F, Kosen S and Karenowska A D 2017 *Sci. Rep.* **7** 11511
[12] Soykal O O and Flatté M E 2010 *Phys. Rev. Lett.* **104** 077202
[13] Zhang D, Wang X M, Li T F, Luo X Q, Wu W, Nori F and You J 2015 *NPJ Quantum Inf.* **1** 15014
[14] Zhang X, Zou C, Jiang L and Tang H X 2016 *J. Appl. Phys.* **119** 023905
[15] Bourhill J, Kostylev N, Goryachev M, Creedon D L and Tobar M E 2016 *Phys. Rev.* B **93** 144420
[16] Osada A, Gloppe A, Hisatomi R, Noguchi A, Yamazaki R, Nomura M, Nakamura Y and Usami K 2018 *Phys. Rev. Lett.* **120** 133602
[17] Cao Y, Yan P, Huebl H, Goennenwein S T B and Bauer G E W 2015 *Phys. Rev.* B **91** 094423
[18] Graf J, Pfeifer H, Marquardt F and Kusminskiy S V 2018 *Phys. Rev.* B **98** 241406
[19] Martínez-Pérez M J and Zueco D 2018 *ACS Photonics* **6** 360–7
[20] Pribiag V S, Krivorotov I N, Fuchs G D, Braganca P M, Ozatay O, Sankey J C, Ralph D C and Buhrman R A 2007 *Nat. Phys.* **3** 498–503
[21] Wintz S, Tiberkevich V, Weigand M, Raabe J, Lindner J, Erbe A, Slavin A and Fassbender J 2016 *Nat. Nanotechnol.* **11** 948–53
[22] Dieterle G *et al* 2019 *Phys. Rev. Lett.* **122** 117202
[23] Rößler U K, Bogdanov A N and Pfleiderer C 2006 *Nature* **442** 797–801
[24] Finocchio G, Büttner F, Tomasello R, Carpentieri M and Kläui M 2016 *J. Phys. D: Appl. Phys.* **49** 423001
[25] Fert A, Cros V and Sampaio J 2013 *Nat. Nanotechnol.* **8** 152–6
[26] Yuan H Y and Wang X R 2016 *Sci. Rep.* **6** 22638

[27] Landau L and Lifshitz E 1992 *On the Theory of the Dispersion of Magnetic Permeability in Ferromagnetic Bodies Perspectives in Theoretical Physics* (Amsterdam: Elsevier) pp 51–65
[28] Gilbert T 2004 *IEEE Trans. Magn.* **40** 3443–9
[29] Shinjo T, Okuno T, Hassdorf R, Shigeto K and Ono T 2000 *Science* **289** 930–2
[30] Kim J V, Garcia-Sanchez F, Sampaio J A, Moreau-Luchaire C, Cros V and Fert A 2014 *Phys. Rev.* B **90** 064410
[31] Gu X, Kockum A F, Miranowicz A, Liu Y-X and Nori F 2017 *Phys. Rep.* **718–719** 1–102
[32] Schleich W P 2001 *Quantum Optics in Phase Space* (New York: Wiley)
[33] Khapaev M M, Kupriyanov M Y, Goldobin E and Siegel M 2002 *Supercond. Sci. Technol.* **16** 24–7
[34] Roy D, Wilson C and Firstenberg O 2017 *Rev. Mod. Phys.* **89**
[35] Vansteenkiste A, Leliaert J, Dvornik M, Helsen M, Garcia-Sanchez F and Waeyenberge B V 2014 *AIP Adv.* **4** 107133
[36] Gladii O, Halley D, Henry Y and Bailleul M 2017 *Phys. Rev.* B **96**
[37] Yu H, d'Allivy Kelly O, Cros V, Bernard R, Bortolotti P, Anane A, Brandl F, Huber R, Stasinopoulos I and Grundler D 2014 *Sci. Rep.* **4** 6848
[38] Dürrenfeld P *et al* 2015 *Phys. Rev.* B **92**
[39] Schoen M A W, Thonig D, Schneider M L, Silva T J, Nembach H T, Eriksson O, Karis O and Shaw J M 2016 *Nat. Phys.* **12** 839–42
[40] Verba R V, Hierro-Rodriguez A, Navas D, Ding J, Liu X M, Adeyeye A O, Guslienko K Y and Kakazei G N 2016 *Phys. Rev.* B **93** 214437
[41] Guslienko K Y 2006 *App. Phys. Lett.* **89** 022510
[42] Krüger B, Drews A, Bolte M, Merkt U, Pfannkuche D and Meier G 2007 *Phys. Rev.* B **76** 224426
[43] Haroche S 2013 *Rev. Mod. Phys.* **85** 1083–102
[44] Auffèves A, Gerace D, Gérard J M, Santos M F, Andreani L C and Poizat J P 2010 *Phys. Rev.* B **81**
[45] Zueco D and García-Ripoll J 2019 *Phys. Rev.* A **99**
[46] Hümmer T, García-Vidal F J, Martín-Moreno L and Zueco D 2013 *Phys. Rev.* B **87**
[47] Jenkins M D, Naether U, Ciria M, Sesé J, Atkinson J, Sánchez-Azqueta C, del Barco E, Majer J, Zueco D and Luis F 2014 *App. Phys. Lett.* **105** 162601
[48] Kittel C 1971 *Introduction to Solid State Physics* (New York: Wiley)
[49] Sampaio J, Cros V, Rohart S, Thiaville A and Fert A 2013 *Nat. Nanotechnol.* **8** 839–44
[50] Boulle O *et al* 2016 *Nat. Nanotechnol.* **11** 449–54
[51] Aranda A, Hierro-Rodriguez A, Kakazei G, Chubykalo-Fesenko O and Guslienko K 2018 *J. Magn. Magn. Mater.* **465** 471–9
[52] Wang X S, Yuan H Y and Wang X R 2018 *Commun. Phys.* **1** 31
[53] Soumah L, Beaulieu N, Qassym L, Carrétéro C, Jacquet E, Lebourgeois R, Youssef J B, Bortolotti P, Cros V and Anane A 2018 *Nat. Commun.* **9** 3355